

Magnetic Reconnection in a Compact Magnetic Dome: Peculiar Emissions and High-velocity Plasma Flows

J. M. DA SILVA SANTOS,¹ E. DUNNINGTON,² R. JAROLIM,³ S. DANILOVIC,⁴ AND S. CRISCUOLI¹

¹*National Solar Observatory, 3665 Discovery Drive, Boulder, CO 80303, USA*

²*Rensselaer Polytechnic Institute, 110 8th St, Troy, NY 12180, USA*

³*High Altitude Observatory, NSF NCAR, 3080 Center Green Dr, Boulder, CO 80301, USA*

⁴*Institute for Solar Physics, Department of Astronomy, Stockholm University, AlbaNova University Centre, 106 91, Stockholm, Sweden*

ABSTRACT

Magnetic reconnection at small spatial scales is a fundamental driver of energy release and plasma dynamics in the lower solar atmosphere. We present novel observations of a brightening in an active region, captured in high-resolution data from the Daniel K. Inouye Solar Telescope (DKIST) using the Visible Broadband Imager (VBI) and the Visible Spectro-Polarimeter (ViSP). The event exhibits Ellerman bomb-like morphology in the H β filter, associated with flux cancellation between a small negative polarity patch adjacent to opposite-polarity plage. Additionally, it displays a distinct annular emission pattern in Ca II K, hot jet-like structures containing Alfvénic plasma flows, and cooler surges. We employ multi-line, non-local thermodynamic equilibrium (non-LTE) inversions of the spectropolarimetric data to infer the stratification of the physical parameters of the atmosphere. Furthermore, we use the photospheric vector magnetogram inferred from the ViSP spectra as a boundary condition for nonlinear force-free field extrapolations, revealing the three-dimensional distribution of squashing factors. We find significant enhancements in temperature, velocity, and microturbulence confined to the upper photosphere and low chromosphere. Our findings provide observational evidence of low-altitude magnetic reconnection along quasi-separatrix layers in a compact fan-spine-type configuration, highlighting the complex interplay between magnetic topology, energy release, and plasma flows. Finally, we discuss the potential role of nonthermal particles in the distinct emissions at different wavelengths.

Keywords: Solar atmosphere (1477) — Solar chromosphere (1479) — Solar magnetic fields (1503) — Spectropolarimetry (1973)

1. INTRODUCTION

Small-scale ($\lesssim 1''$) magnetic reconnection events are fundamental and dynamic processes shaping the lower solar atmosphere. These events, which often result from complex interactions of opposite magnetic polarities, are observed as transient (lasting from a few seconds to a few minutes), dot-like or elongated brightenings across multiple spectral bands from ultraviolet (UV) and visible wavelengths (e.g., Georgoulis et al. 2002; Peter et al. 2014; Vissers et al. 2015; Tiwari et al. 2019) to the millimeter continuum (da Silva Santos et al. 2020). Despite their small scale, these phenomena have implications for understanding larger solar processes, such as solar eruptions, while offering a unique opportunity to investigate the physics of magnetic reconnection.

Ellerman bombs (EBs; Ellerman 1917) serve as prototypical examples of magnetic reconnection in the photosphere. Observationally, they are characterized by enhanced, flickering emissions in the wings of hydrogen Balmer and Ca II lines, and they are usually located between or near magnetic bipoles (Rutten et al. 2013, and references therein). UV bursts (UVBs) belong to an analogous broad class of events, notably characterized by brightenings displaying broad line profiles in transition region temperature lines. These profiles exhibit velocities of a few hundred km s⁻¹, comparable to the Alfvén speed, while the chromospheric lines are also enhanced (Young et al. 2018, and references therein). Numerical and observational studies suggest that EBs and UVBs represent different manifestations of a shared underlying process, with variations in the height and physical conditions of the reconnection site, as well as the viewing angle, determining their spectral signatures and co-occurrence (e.g., Hansteen et al. 2017, 2019; Chen et al. 2019; Ortiz et al. 2020; Skan et al. 2023).

Key open questions in the study of EBs/UVBs center on understanding the magnetic topology and nature of the reconnection processes, as well as explaining the dynamics of the observed outflows. For example, the tearing mode instability, or plasmoid-mediated reconnection, in which the current sheet fragments into smaller magnetic islands (reviewed in Pontin & Priest 2022), has been proposed to explain multi-component velocities in spectroscopic observations (Innes et al. 2015) and the intermittency of UV emissions (Peter et al. 2019). High-resolution ground-based observations have occasionally resolved the sources of this intermittency into fine-scale ($\sim 0.1''$) recurrent plasmoid-like bright blobs, which appear to be ejected from reconnection sites (Roupe van der Voort et al. 2017, 2023; Díaz Baso et al. 2021). Alternatively, turbulent reconnection driven by the Kelvin-Helmholtz instability has been suggested as a more plausible mechanism in certain contexts, given the large apparent size of the reconnection region in some EB events (Anan et al. 2024). Enhanced turbulence has also been invoked to explain excess line widths attributed to turbulent motions within the reconnection region in UV brightenings (e.g., Wu 2019; Chitta & Lazarian 2020; Ortiz et al. 2020).

With regard to the magnetic topology, U-type (concave-up) configurations, where the reconnection occurs in bald patch separatrixes (Titov et al. 1993), are typically consistent with observations of EBs (e.g., Georgoulis et al. 2002; Pariat et al. 2004, 2009). The same configuration has been proposed to explain some UVBs (Peter et al. 2014; Zhao et al. 2017). However, in some instances, UVBs appeared to be triggered at magnetic null points at the top of magnetic domes in fan-spine configurations (Chitta et al. 2017). This configuration has also been observed in larger-scale flares exhibiting circular flare ribbons (e.g., Masson et al. 2009; Wang & Liu 2012; Sun et al. 2013), which suggests a link between the weakest and strongest reconnection events (Smitha et al. 2018). Recently, a study of a large sample of quiet-Sun EBs and associated UV brightenings reported a range of magnetic configurations, spanning from simple bipoles to fan-spine topologies, where the EB and UVB components originate from different parts of the 3D magnetic structures, as inferred from potential field extrapolations (Bhatnagar et al. 2024).

In this study, we present the analysis of a small-scale brightening observed in an active region (AR) with the Daniel K. Inouye Solar Telescope (DKIST; Rimmele et al. 2020). We derive the atmospheric parameters of the event through multi-line non-local thermodynamic equilibrium (NLTE) inversions and perform non-linear force-free field (NLFFF) extrapolations based on a high-resolution ViSP magnetogram, complementing the previous topological studies and providing new observational insights into the impact of magnetic reconnection in the low atmosphere.

2. DATA

2.1. Data Acquisition and Post-processing

We used imagery provided by the Visible Broadband Imager (VBI; Wöger et al. 2021) and spectropolarimetric data acquired by the Visible Spectro-Polarimeter (ViSP; de Wijn et al. 2022) instruments at the DKIST. The target was AR NOAA 13465 close to the disk center at $\mu \sim 0.99$, where μ is the cosine of the heliocentric angle, on 2023 October 16. The observing campaign consisted of multiple ViSP scans of different sub-fields around the AR both in spectroscopy and polarimetry modes supported by VBI imaging (Schad et al. 2025). Here, we focused on a particular pointing centered on the sunspot at helioprojective coordinates $\sim [-76'', 90'']$ between 20:18–20:38 UT in polarimetry mode. We also used line-of-sight (LOS) magnetograms provided by the Helioseismic and Magnetic Imager (HMI; Scherrer et al. 2012) and EUV and UV images taken by the Atmospheric Imaging Assembly (AIA; Lemen et al. 2012) on board the Solar Dynamics Observatory (SDO; Pesnell et al. 2012).

The VBI data comprise high-resolution broad-band images in the G-band (4305 Å), H β (4861 Å), and Ca II K (8500 Å) filters. The VBI acquired sequences of 80 images with single exposure times of 0.7 ms, 3.5 ms, and 25 ms for the G-band, H β , and Ca II K filters, respectively. The VBI operated at a higher cadence of 2.7 s in the G-Band filter, interspersed with a lower cadence sub-cycle in the other filters every fifth image. The cadence for Ca II K and H β was 19.8 seconds. The image scale is approximately 0.0106'' per pixel. The filters' full width at half maxima (FWHM) are approximately 4.37 Å, 0.46 Å, and 1.01 Å, for G-band, H β , and Ca II K filters, respectively. As part of the reduction pipeline, the images were dark- and gain-corrected and processed using a speckle algorithm to remove seeing-induced distortions (Wöger et al. 2008). The units are in detector counts. We coaligned the VBI and SDO data via cross-correlation between the VBI G-band images and the HMI 6173 Å continuum images, and we coaligned VBI and ViSP by cross-correlating the G-band images and the 6301 Å continuum images from the ViSP. Additionally, we cross-correlated the VBI channels among themselves to correct for measured relative misalignments on the order of $\sim 0.1''$ – $0.2''$, consistent with wavelength-dependent atmospheric dispersion (Reardon 2006).

The ViSP data consist of a single spectropolarimetric raster scan in three passbands, approximately 13–18 Å wide, centered on the Fe I 6301 and 6302 Å lines (hereafter $\lambda 6301(2)$), the Na I D₁ 5896 Å line (hereafter $\lambda 5896$), and the Ca II 8542 Å line (hereafter $\lambda 8542$). The raster maps covered an area of about $46'' \times 76''$ in $\lambda 6301(2)$, $46'' \times 61''$ in $\lambda 5896$, and $46'' \times 49''$ in $\lambda 8542$ encompassing the sunspot. The raster step was $\sim 0.1''$. The pixel scale along the slit varies be-

tween the three arms; for analysis purposes, we rebinned the spectra (factors of $\sim 3\text{--}5$) to $0.1''$ square pixels. Then, we co-aligned the three arms by cross-correlation of continuum images from each arm. The number of modulation states and cycles was 10, requiring ~ 3 s per slit position, resulting in a total raster time of approximately 20 minutes. We estimated the polarimetric sensitivity to be on the order of $(6\text{--}8)\times 10^{-4}$ relative to the continuum, with better signal-to-noise ratio in the photospheric passbands.

The ViSP data were reduced with version 2.10.7¹ of the calibration pipeline, which includes dark and gain corrections, as well as polarization calibration. We further corrected for residual polarization crosstalk using standard methods (Sanchez Almeida & Lites 1992). The wavelength and absolute intensity calibrations were performed via cross-correlation of the average spectra with the solar atlas of Neckel & Labs (1984). This included an optimization procedure to improve the dispersion values upon what is provided in the Level 1 file headers using the wavelength positions of the telluric lines as a reference. We obtained approximately 0.014 \AA , 0.013 \AA , and 0.019 \AA for the $\lambda 5896$, $\lambda 6301(2)$, and $\lambda 8542$ passbands, respectively.

The level 1 AIA data were converted into level 1.5 with the `aia_prep` routine in SolarSoftware (Freeland & Handy 1998). We show AIA 1700 \AA and 304 \AA images taken at a cadence of 24 s and 12 s, respectively. The image scale is $0.6''$ per pixel. The HMI LOS magnetograms have a cadence of 45 s and image scale of $0.5''$ per pixel. We also used one 720 s-cadence vector magnetogram taken at 20:34 UT that was processed with the SHARP pipeline (Bobra et al. 2014).

2.2. Target Overview

Figure 1 presents an overview of the target. Panels (a) and (b) show SDO/HMI observations, providing a contextual view of the AR, which is only partially captured by DKIST. The magnetic flux density distribution in the field of view (FOV) is dominated by the sunspot’s positive polarity, surrounded by plage regions and pores of opposite polarity. DKIST/ViSP observations zoom into the region enclosed by the dashed box in (a). Panels (c) and (d) show the ViSP LOS magnetogram obtained using Milne-Eddington inversions of the $\lambda 6301(2)$ lines (described in Section 4.2), and the 6301 \AA continuum intensities for direct comparison with (a) and (b), showing a good agreement. While the raster map is affected by periods of poor seeing, the subregion within the blue box – the primary focus of this paper, clearly reveals a small negative polarity patch ($\lesssim 1''$) near a pore of positive polarity. This negative patch is barely distinguishable in the HMI magnetogram. Panel (e) shows the intensity map in the core of $\lambda 8542$, revealing the opaque chromospheric fibrils.

Panels (f)–(h) present the images from DKIST’s VBI taken at a specific time within the ViSP raster interval. The G-band image shows very fine details of the penumbrae and the magnetic elements associated with the bright points. The $\sim 0.46 \text{ \AA}$ wide $H\beta$ filter captures both the photosphere and chromosphere, revealing fibril structures extending outward from both penumbrae and plage regions. Finally, the Ca II K images also provide a combined view of the photosphere and chromosphere but with higher chromospheric opacity than $H\beta$. The arrows in these panels mark the brightenings analyzed in this study, which occur at the interface between opposite magnetic polarities. The blue box in panels (c)–(e) defines the region of interest (ROI).

3. METHODS

3.1. Spectropolarimetric Inversions

To obtain the magnetic field at different heights, we began by applying two different inversion techniques to the spectropolarimetric data, focusing on the main spectral diagnostics within the three ViSP arms. We employed the Milne-Eddington (ME) approximation to the $\lambda 6301(2)$ lines using the `pyMilne` code (de la Cruz Rodríguez 2019), and we applied the Weak Field Approximation (WFA) to the cores of $\lambda 5896$ and $\lambda 8542$ lines using the `spatial_WFA` code (Morosin et al. 2020). The resulting magnetic field estimates can then serve as inputs for more detailed NLTE inversions (see below) or magnetic field extrapolations (Section 3.2).

The inversions of $\lambda 6301(2)$ successfully retrieved the magnetic field components in the photosphere; the LOS magnetogram derived from $\lambda 6301(2)$ is displayed in Fig. 1c. We further resolved the magnetic azimuth angle ambiguity using the minimum energy method with the `AMBIG` code (Leka et al. 2014). We verified that the resulting magnetic vector components were generally consistent with the cotemporal, lower resolution SHARP maps. The WFA inversions, however, lacked consistency in parts of the sunspot umbra, likely due to the high field strengths ($\gtrsim 2 \text{ kG}$). As this could negatively impact the extrapolations, we excluded the $\lambda 5896$ and $\lambda 8542$ WFA inversion maps from subsequent analysis. However, we still include those lines in the NLTE inversions of the ROI, as the field strength is not a constraint for this method.

We performed NLTE inversions using the SStockholm inversion Code² (`STiC`; de la Cruz Rodríguez et al. 2016, 2019), which is a massively parallel, multi-atom inversion code based on a modified version of the Rybicki & Hummer (RH; Uitenbroek 2001) radiative transfer code. The atomic models used in the statistical equilibrium calculations included a 11-level atom for Na I plus a Na II continuum level, and a 5-level model for Ca II plus a Ca III continuum level.

¹ <https://docs.dkist.nso.edu/projects/visp/en/v2.10.7/>

² <https://github.com/jaimedelacruz/stic>

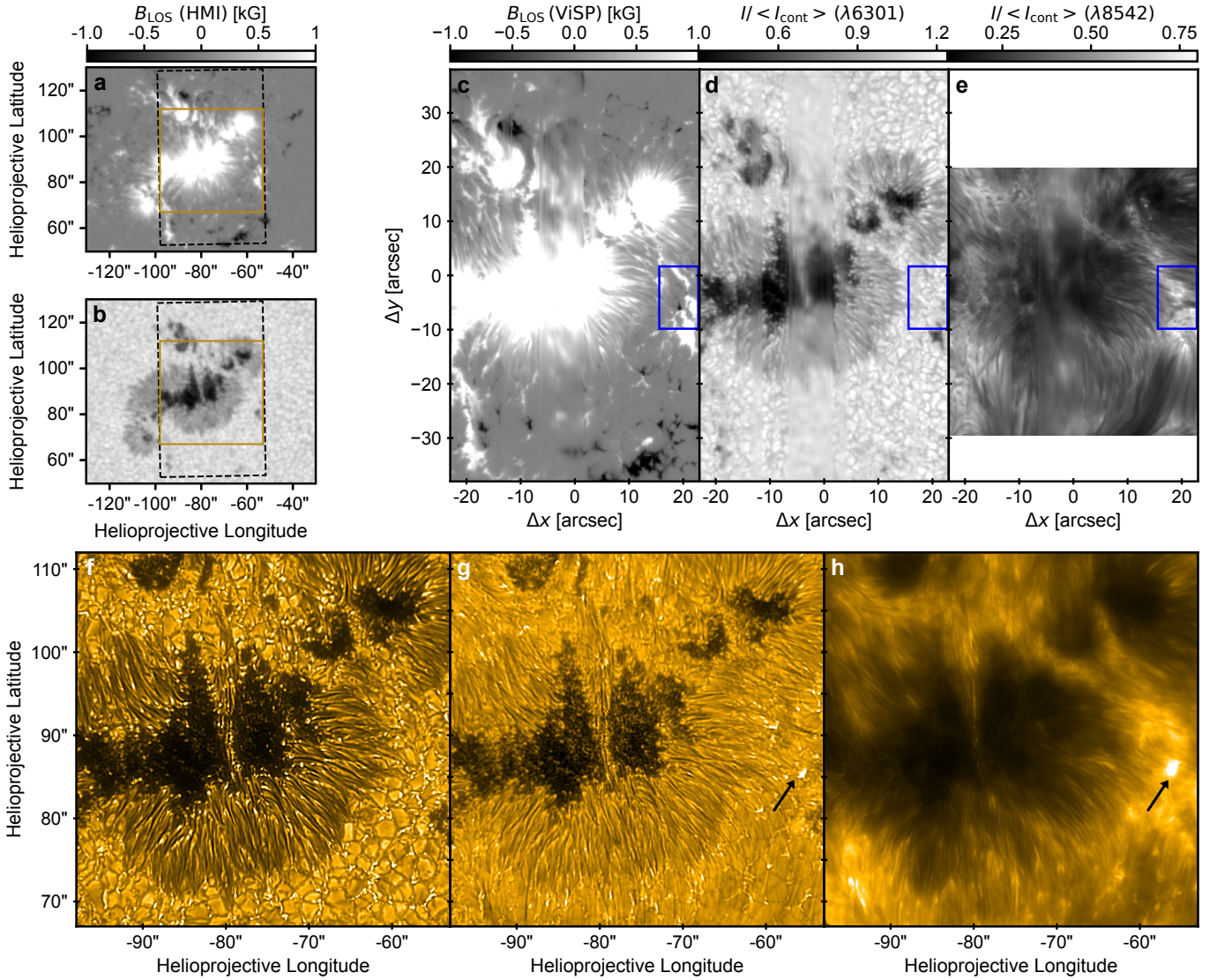


Figure 1. Overview of AR 13465 on 2023 October 16. (a): SDO/HMI LOS magnetogram. (b): SDO/HMI 6173 Å continuum. (c): DKIST/ViSP photospheric LOS magnetogram obtained with `PyMilne`. (d): DKIST/ViSP raster in the 6301 Å continuum. (e): DKIST/ViSP Ca II 8542 Å core. (f): DKIST/VBI G-band. Panel (g): DKIST/VBI H β . (h): DKIST/VBI Ca II K. All colormap ranges are capped for display purposes. The dashed and solid boxes in (a)–(b) show the ViSP ($\lambda 6301(2)$) and VBI fields of view, respectively. The blue boxes in panels (c)–(e) show the region selected for the NLTE inversions (Fig. 5). The arrows indicate the brightening that is focus of study here.

The Fe I 6301 and 6302 Å lines were treated in LTE. For expediency, hydrogen was treated in LTE, which is a fair assumption in the layers probed by the $\lambda 5896$ and $\lambda 8542$ lines from an inversion standpoint (da Silva Santos et al. 2024).

We considered incorporating additional weak photospheric lines of Fe I (5892.7, 5898.2, 8538 Å), Si I (8536.1 Å), Ni I (5892.9 Å), and Ti I (8548.1 Å) within the ViSP passbands using atomic data from the Kurucz database³. However, inversion tests with the AR data showed systematic misfits in intensity (and sometimes wavelength) to these lines to varying degrees, suggesting atomic data inaccuracies. Therefore,

³ <http://kurucz.harvard.edu/>

we excluded these lines from the inversions, fitting only the strongest lines in each ViSP arm. Nonetheless, we included them in spectral synthesis to assess how well they are predicted by the inferred models.

The inversion process followed a standard multi-cycle approach, progressively increasing the number of nodes to improve the fit. Here, we ran three cycles with eight nodes for temperature, increasing up to six nodes for line-of-sight velocity and microturbulence, and up to four nodes for the line-of-sight and transverse components of the magnetic field, as well as the azimuth angle. Increasing the number of nodes beyond this did not significantly improve the quality of the fits. We employed the ME inversion maps mentioned above as an initial guess for the magnetic field stratification and we

used the F99 model (Fontenla et al. 1999) as an initial guess for the temperature stratification. F99 reproduces the (average) QS atlas profiles of $\lambda 5896$ and $\lambda 8542$ quite well using the aforementioned atomic models. We present the synthesis of these lines from F99 alongside the brightening line profiles to highlight their differences from QS.

3.2. Magnetic Field Extrapolations

We performed NLFFF extrapolations based on photospheric vector magnetograms to estimate the 3D topology of the AR. To this aim, we applied the method⁴ developed by Jarolim et al. (2023), which employs a Physics Informed Neural Network (PINN; Raissi et al. 2019) to estimate the 3D magnetic field, \vec{B} . An iterative optimization scheme was used to satisfy the boundary conditions and enforce the force-free equations ($\nabla \cdot \vec{B} = 0$; $\nabla \times \vec{B} \times \vec{B} = 0$). This approach has shown the ability to flexibly find a trade-off between noisy observational data and the incomplete physical model, providing realistic approximations of the coronal magnetic field (cf., Purkhart et al. 2023; McKeivitt et al. 2024; Korsós et al. 2024; Jarolim et al. 2024b). We made use of the mesh-free simulation volume which allows us to flexibly embed a high-resolution DKIST/ViSP vector magnetogram as part of the AR (inferred from the $\lambda 6301(2)$ observations) into the lower resolution, but more extended, SDO/HMI vector magnetogram (i.e., the SHARP maps in cylindrical equal area projection). This is essential for accurately modeling the field connectivity within the global topology of the AR. Therefore, we can estimate the small scale magnetic field structure of the ViSP observation in the ROI, while simultaneously obtaining the global magnetic topology of the AR magnetic field. Per updating step, we randomly sampled 2^{13} points from both the SHARP map at 360 km per pixel resolution and the DKIST/ViSP observation at 72 km per pixel resolution. Here, we masked out the ViSP FOV from the SHARP map. Similarly to Jarolim et al. (2023), we continuously sampled 2^{14} random points from the simulation volume. Per updating step, we optimized both for the sampled boundary conditions and minimized the deviation from the partial differential equations $\nabla \cdot \vec{B} = 0$, $\nabla \times \vec{B} \times \vec{B} = 0$, where we weight the SHARP boundary condition with 1 and the divergence and force-free equations with 10^{-2} . For the ViSP boundary condition, we set the weighting factor to 1 and exponentially increase the weight to 10 over 5×10^4 iterations. The optimization was performed over 2×10^5 iterations until convergence was reached.

The magnetic field solution can be sampled at arbitrary resolution from the resulting neural representation. For further evaluation, we sampled a frame spanning $30 \times 30 \text{ Mm}^2$ around the negative polarity, with a resolution of 72 km per

pixel. We computed the current density, $\vec{J} = (c/4\pi)\nabla \times \vec{B}$ (where c is the speed of light), using smooth derivatives from the neural representation. Additionally, we computed the squashing factor, Q , and the twist number, \mathcal{T}_w , for each point in the resulting 3D volume using the FastQSL⁵ method (Zhang et al. 2022). The squashing factor is used to characterize the magnetic topology, where a large Q indicates that local regions experience a strong divergence of magnetic field lines (e.g., Titov 2007). The twist number is a measure of how many turns two infinitesimally close magnetic field lines make around each other (Berger & Prior 2006) and is used to identify variations in helicity.

4. RESULTS

4.1. Observational Characteristics

Figure 2 presents selected time frames of the brightening observed by AIA, along with the magnetic flux variation from HMI magnetograms over a longer time span than DKIST observations. The image sequences were corrected for solar rotation. The magnetic flux, Φ , was calculated within a $3.5'' \times 3.5''$ region centered on the negative polarity patch concentration at 19:40 UT (blue box). The HMI magnetograms reveal the emergence of a small-scale negative polarity patch, moving approximately radially outward from the sunspot penumbra in the southeast direction. This motion is characteristic of moving magnetic features (MMFs). The patch enters a predominantly positive polarity region, with the negative magnetic flux reaching its maximum around 19:40 UT. Using centroid tracking and an uncertainty of half the AIA image scale, we measured its plane-of-sky velocity as $1.8(\pm 0.3) \text{ km s}^{-1}$, consistent with typical MMF speeds (e.g., Hagenaar & Shine 2005; Li et al. 2019a).

By the time DKIST began observing ~ 20 min later, the negative polarity patch had become almost indistinguishable (top panels), though it remains visible in the ViSP magnetogram (cf. Fig. 1c). Still, significant variations in the magnetic flux could be measured from HMI (bottom panel in Fig. 2). The total magnetic flux within the blue box decreased steadily over the course of an hour at an average rate of $d\Phi/dt \sim 10^{19} \text{ Mx h}^{-1}$, that is $\sim 3 \times 10^{15} \text{ Mx s}^{-1}$, comparable to reported flux cancellation rates in ARs (e.g., Reid et al. 2016; Tian et al. 2018; Chitta et al. 2020).

The appearance of the opposite polarity was followed by a significant increase in the 1700 \AA continuum emission between the two polarities, albeit with a temporal offset. Through cross-correlation, we determined a lag of approximately 11.3 min between the peak AIA intensities and the negative magnetic flux, with a linear correlation coefficient of $r = 0.75$. We find no significant enhancements in the hotter

⁴ <https://github.com/RobertJaro/NF2>

⁵ <https://github.com/peijin94/FastQSL>

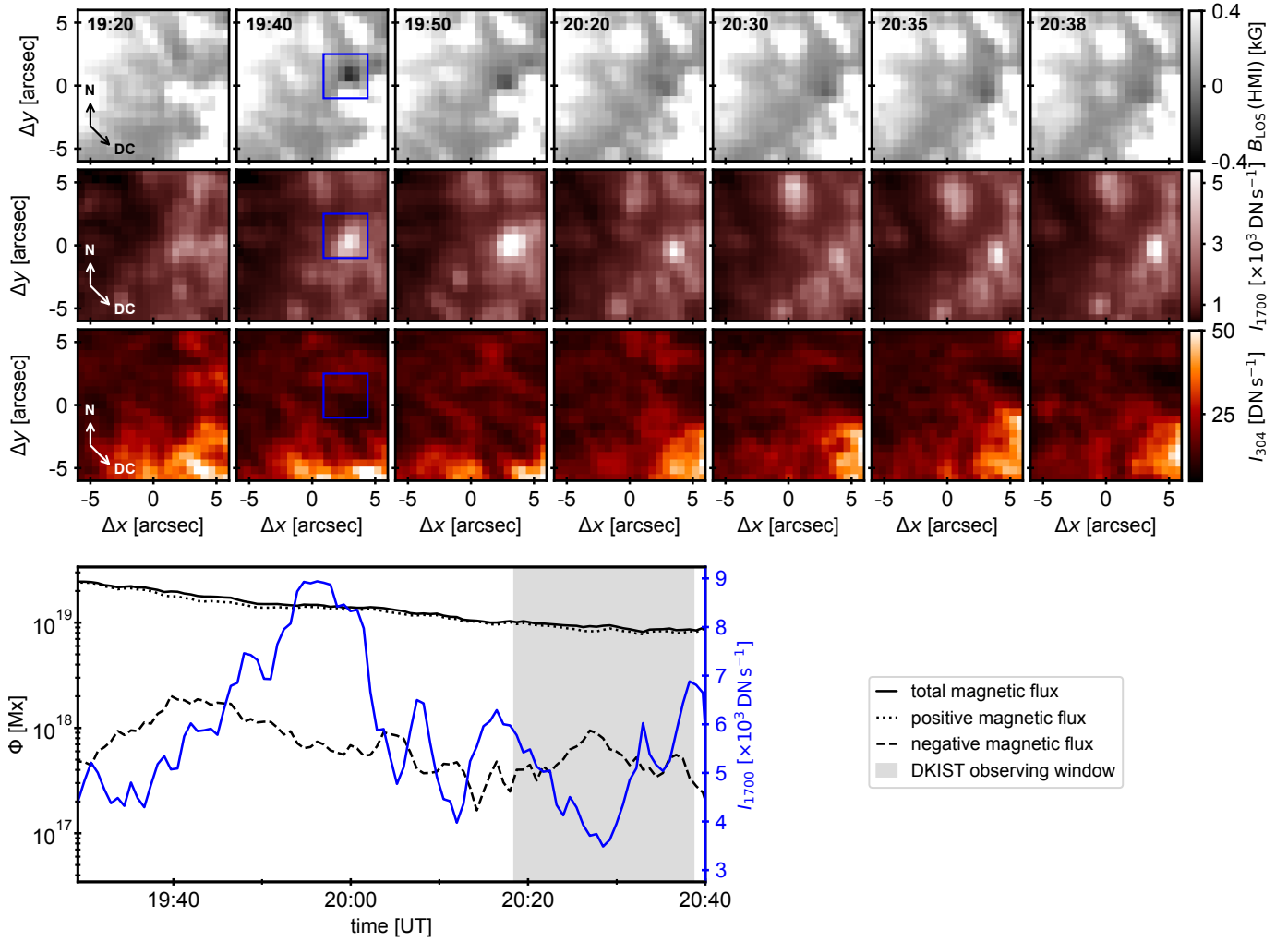


Figure 2. Time evolution of the brightening captured by SDO. The small panels show, from the top to the bottom, HMI line of sight magnetograms capped at ± 0.4 kG, and intensities in the AIA 1700 Å and 304 Å channels of the brightening highlighted in the bottom panels in Fig. 1; the arrows indicate the directions of solar north and disk center. The bottom left panel shows the time variation of total, positive, and negative magnetic fluxes and maximum AIA 1700 Å intensities within the region enclosed by the blue box in the top panels.

AIA channels (e.g. 171 Å, 94 Å) at the same location. However, we do observe a dimming in AIA 304 Å (bottom panels), which could be due to absorbing cool material ejected into the upper atmosphere.

4.1.1. Photospheric Dynamics in High Resolution

Figure 3 displays selected time frames of the VBI time series data in the same FOV as in Figure 2. We also provide a supplementary movie showing the time evolution in greater detail. The VBI images resolve finer details of the brightenings compared to AIA, showing EB-like “flame” structures in the $H\beta$ filter (e.g., Libbrecht et al. 2017; Joshi et al. 2020) in two different events within the top right quadrant of the FOV (e.g., 20:30 UT). The EB classification is corroborated by enhanced AIA 1700 Å emissions at the same locations (e.g., Vissers et al. 2013, 2019; Danilovic et al. 2017), as shown in Fig. 2. The northernmost EB candidate is short-lived, lacks a Ca II K counterpart, and does not appear to be

linked to a photospheric magnetic bipole. We therefore focus on the southernmost event, which corresponds to the AIA brightening within the blue box in Fig. 2 and displays more distinct characteristics. The evolution of substructures in the ROI (red arrow) resembles small-scale ($\sim 0.1''$ – $0.4''$) moving blobs, interpreted as plasmoids in rare high-resolution observations of similar events in the $H\alpha$ line (Roupe van der Voort et al. 2023), the Ca II K line (Roupe van der Voort et al. 2017; Díaz Baso et al. 2021), and more recently in the He I 10830 Å line (Leenaarts et al. 2025).

G-band images reveal fine “filigree” (Dunn & Zirker 1973) structures at the location of the southernmost EB candidate. As bright filigree converge at the apex of several granules and the granules evolve, the flame-like feature in $H\beta$ changes morphology. This phenomenon has been reproduced by high-resolution simulations, showing that flames outline current sheets forming where complex magnetic structures are

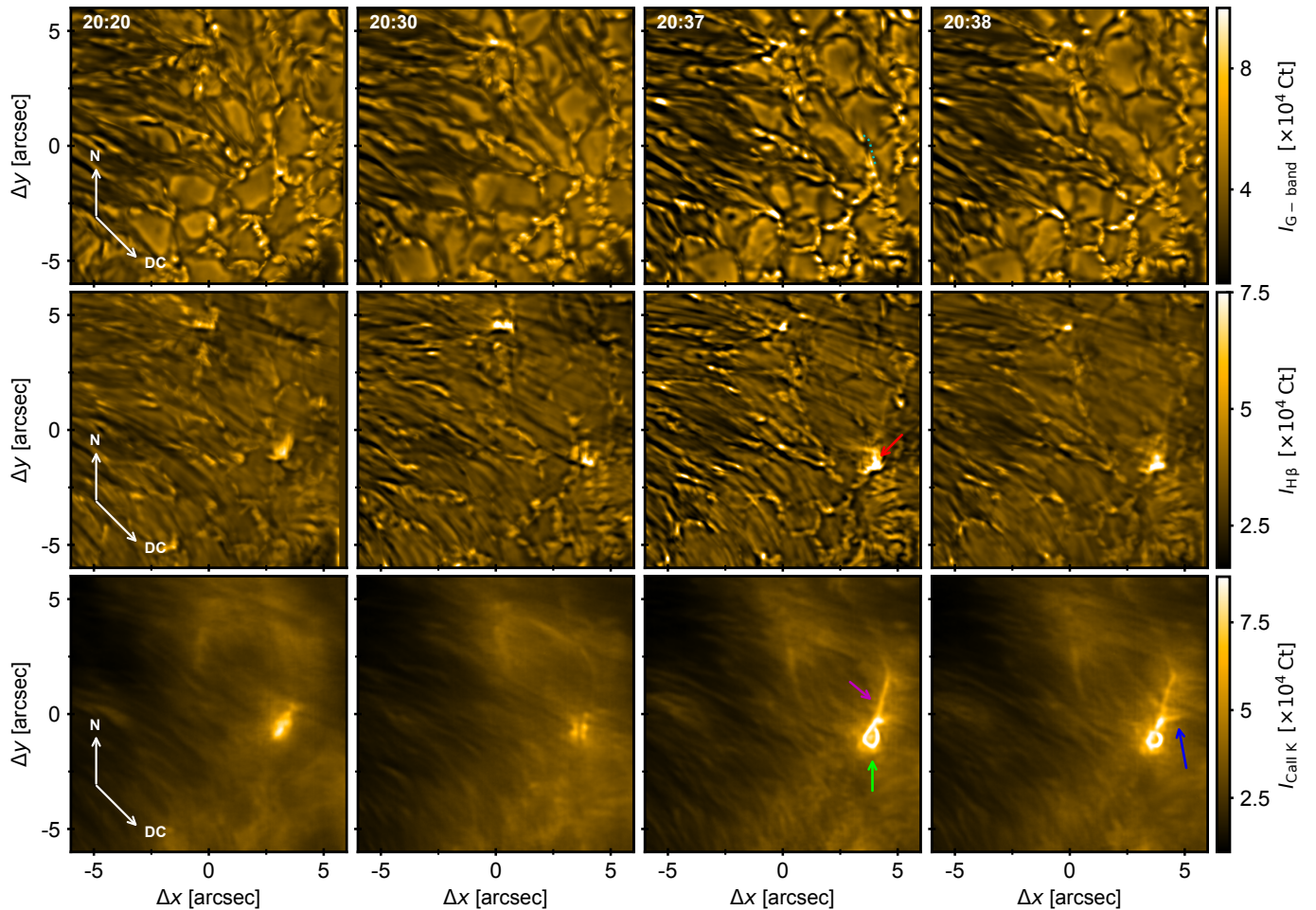


Figure 3. High-resolution view of the event provided by DKIST/VBI. From the top to the bottom, intensities (in counts) in the VBI G-band, $H\beta$ and Ca II K filters. The FOV is the same as in Fig. 2. The white arrows indicate the directions of solar north and disk center. The colored arrows point to different features of interest (see text).

compressed (Danilovic 2017; Danilovic et al. 2017). The G-band movie shows that around 20:28 UT, granules extend northwest from the $H\beta$ structure. Bright magnetic elements rapidly approach from the northwest (parallel to the cyan dotted line, Fig. 3 20:37 UT), with plane-of-sky velocities of approximately $\sim 4\text{--}6\text{ km s}^{-1}$. This indicates that the new magnetic flux is advected towards the same location. When one of the bright G-band points merges with the filigree at the site of the $H\beta$ enhancement, a distinct circular structure appears in the Ca II K filter.

4.1.2. A Peculiar Annular Brightening

The brightening in the Ca II K filter initially appears as a diffuse blob, spatially offset from the $H\beta$ enhancement in the limb-ward direction. Later, a bright ring (green arrow) appears connected to a bright fibril-like structure (magenta arrow) oriented orthogonally to the dark fibril background. There is also an enhancement at the center of the ring. Gaussian fitting of the ring’s transverse profile yields an annulus FWHM of $\sim 0.11''$. We find the annular structure particu-

larly intriguing, as we are not aware of similar features being reported in the ground-based literature at comparable resolution. Furthermore, the VBI observations also reveal jet-like structures with projected widths of $\sim 0.2''$ (blue arrow) forming at an angle to the bright fibril-like structure. The bright fibril is also visible in the $H\beta$ images but appears much dimmer; for example, compare 20:30 and 20:37 UT.

The time evolution of the annular structure is better appreciated in the supplemental movie, showing a series of expansions and contractions over time. To quantify its morphology variations, we employed a non-linear least-squares fitting routine to the brightest pixels along the ring, using an ellipse function to determine its apparent size.

Figure 4 shows the results of this procedure for different time stamps, beginning when the ring first appears and continuing until seeing conditions degrade. We find that the equivalent diameter (twice the geometric mean of the semi-major and semi-minor axes) of the ring initially expands from approximately $0.45''$ to $0.65''$ over 60 sec. It then contracts to about $0.4''$ before expanding again to around $0.55''$ toward

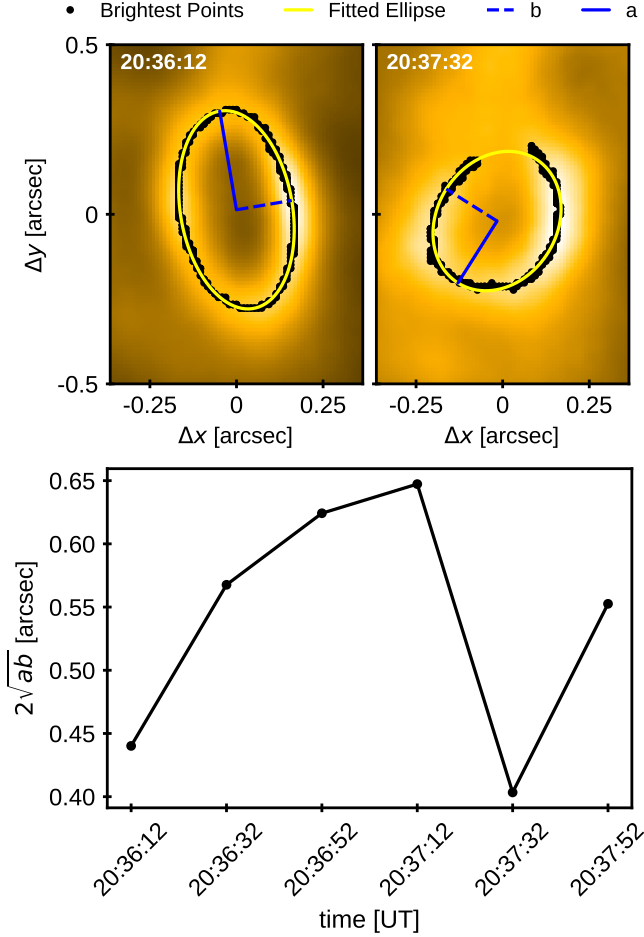


Figure 4. Ellipse fitting to the ring emission. Top panels: VBI Ca II K images at two time steps, showing the brightest points along the ring structure (black dots) and the fitted ellipses characterized by the semi-major axis, a , and semi-minor axis, b . Bottom panel: Temporal evolution of the equivalent diameter of the fitted ellipses.

the end of the time series. Its orientation also changes over time, as shown in the top panels. The configuration of the G-band bright points roughly mirrors the variations in ring size, implying that the photospheric footpoints associated with the ring feature may be confined to a region of only 1–2". The continuous inflow of magnetic bright points throughout the evolution of the Ca II K structures may account for the deposited energy, as it introduces magnetic flux at high horizontal velocity. We further explore the magnetic topology of the event in Section 4.3.

4.2. NLTE Inversions

Figure 5 presents the results of the NLTE inversions of the ROI at three different optical depths. We note that we cannot infer the atmosphere parameters beyond $\log \tau \sim -4.5$ from these observations, as the line response functions are weak at lower optical depths. For context, we also show the ViSP intensities in the $\lambda 5896$ and $\lambda 8542$ line cores and

blue wing of $\lambda 8542$ (leftmost panels), as well as VBI intensity contours outlining the shape of the brightenings (at about half-maximum level) in Ca II K (green) and H β (magenta) at 20:37 UT (cf. Fig. 3) when the ViSP slit was scanning the region (see ViSP arrow of time at the bottom). In the discussion below, we also refer to the complementary Fig. 6 showing the inversion results in greater detail for three selected locations: (A) at the center of the H β brightening, (B) at the upper part of the ring brightening, and (C) at an absorbing feature in $\lambda 8542$.

The bright annular structure observed in the Ca II K images (Fig. 3) is not visible in the ViSP raster image in the $\lambda 8542$ core (bottom left in Fig. 5), but can be partially observed at different wavelengths in the line wings (e.g., middle row). We note, however, that the $\lambda 8542$ core intensities within the VBI contours are enhanced relative to the QS level. The significant temporal evolution of the structure under the moving ViSP slit likely distorts the ring emission in the raster image.

4.2.1. Magnetic Field and Temperature Stratifications

The B_{LOS} map in the photosphere clearly shows the small minority (negative) magnetic polarity patch, unlike the co-temporal HMI magnetogram of the same region (cf. Fig. 2). The H β brightening is located between the two opposite polarities, while the Ca II K brightening is spatially offset in the limb-ward direction, but it partly overlaps with the EB. The ring structure is approximately centered on the negative polarity and traces a semi-circular polarity inversion line (PIL). While the magnitude of the B_{LOS} component of the minority negative polarity patch reaches up to 1300 G at $\log \tau = -2$, it practically vanishes in higher layers, with the magnetograms showing an essentially unipolar field for optical depths lower than $\log \tau \sim -4$. However, the polarimetric sensitivity of these ViSP observations is insufficient to reliably determine the chromospheric vector field at a spatial resolution of 0.1", as the transverse field component (and azimuth angle; not displayed) is affected by noise; however, high-resolution is clearly needed to resolve the fine-scale structures of the event, as highlighted by the VBI image sequences.

We find significant temperature enhancements in the photosphere around $\log \tau = -2$, coinciding with broadband intensity enhancements in the VBI filters. The temperature enhancements range from ~ 100 –1,000 K in the lower part of the ring structure (e.g., location A) to just over 2,000 K in the bright kernel at the top (e.g., location B) relative to the QS model. Temperatures also increase at the center of the ring structure in somewhat higher layers around $\log \tau = -3$, which can be interpreted as heating occurring in a dome-like structure. However, the inversion maps are particularly noisy at this depth due to the weak sensitivity of all diagnostics. Lower optical depths layers in the chromosphere ($\log \tau \sim -4.5$) do not show significant tempera-

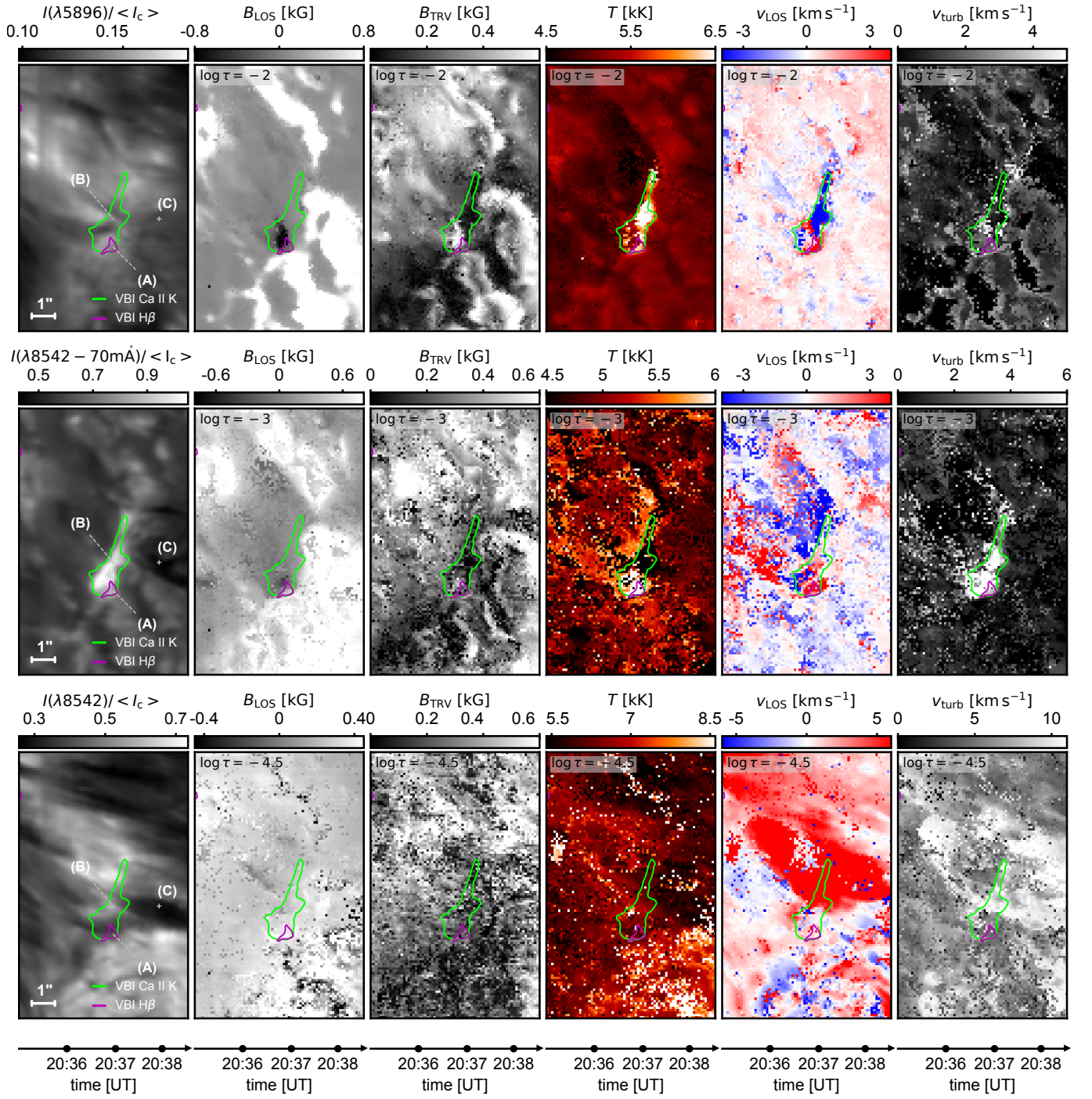


Figure 5. Atmospheric stratification from NLTE inversions. The leftmost panels display the intensities in the $\lambda 5896$ core, as well as core and blue wing of $\lambda 8542$ observed by the ViSP within the blue box shown in Fig. 1(c–e). The green(magenta) contours outline the brightness enhancements in the VBI Ca II K (H β) images at 20:37 UT (cf. Fig. 3). The other panels, from left to right: LOS and transverse components of the magnetic field, temperature, LOS velocity, and microturbulence at three different optical depths. The y-axes are aligned with solar north. The colormaps ranges are capped for display purposes. The timestamps corresponding to particular slit positions are shown at the bottom.

ture enhancements, suggesting that the energy release is quite deep-seated. Consequently, the brightenings observed in the broad-band Ca II K and H β images (Fig. 3) are likely dominated by emission from the line wings, originating in the upper photosphere and lower chromosphere. This is also evident from the $\lambda 8542$ profiles at locations (A) and (B) displayed in Fig. 6, which show strong wing emissions but relatively weaker core enhancements compared to the QS profile. The temperature stratifications at these locations show broad bumps at optical depths (~ 2 dex) in the photosphere.

We also calculated the radiative energy losses in the brightenings from our inversion models following Díaz Baso et al. (2021), and found values reaching up to $\sim 70 \text{ kW m}^{-2}$ in the low chromosphere, integrated between the T_{\min} height and the formation height of $\lambda 8542$ core, with an uncertainty on the order of 15% (da Silva Santos et al. 2024). This value is several times higher than the canonical cooling rates in the low chromosphere in ARs ($\sim 10 \text{ kW m}^{-2}$; Withbroe & Noyes 1977). However, at some locations, the temperature enhancements begin in deeper layers around $\log \tau \sim -1$ (e.g., location A and B). If we integrate the cooling rates from these depths, the total losses could increase by up to an order of magnitude due to the higher densities in the photosphere. For a brightening size of $1''$ and duration of 5 min, the total radiative energy would be $\sim 10^{27}$ erg (see also Fang et al. 2006). Using the same size as a characteristic length, L , and the measured flux cancellation rate from HMI over the same duration (Section 4.1), the magnetic energy, $B\Phi L/(8\pi)$, is of the same order $\sim 10^{27}$ erg (see also Chitta et al. 2020).

4.2.2. Enhanced Velocities and Microturbulence

The LOS velocity maps at the same optical depths show that most of the ring structure is down-flowing, whereas the compact bright ring kernel and bright jet-like structures are mostly up-flowing, forming a bidirectional flow pattern at $\log \tau \sim -2$. Inferred velocities at this depth reach supersonic values up to $\sim 28 \text{ km s}^{-1}$ in the lower part of the ring where the EB brightenings are also located, between the two opposite polarities, and up to $\sim -18 \text{ km s}^{-1}$ in the upper structures. Location (A) is one such cases, showing velocities peaking at $\sim 20 \text{ km s}^{-1}$ at $\log \tau = -2$ (Fig. 6). These velocity magnitudes are on the order of the Alfvén speed at that optical depth. The chromospheric velocities (lower panel in Fig. 5) do not show any coherent structures associated to the brightenings other than an extended downflow patch in the upper part of the FOV. However, the inferred velocity maps do not capture the complete picture.

At location (C), for example, the inversions cannot fit the $\lambda 8542$ profiles associated to the dark structures visible in line wings and core. We observe a depression in the blue wing of $\lambda 8542$ at about $\sim -31 \text{ km s}^{-1}$ (vertical dashed line) relative to nominal line center, while the $\lambda 5896$ line lacks that feature

(Fig. 6). We interpret this as part of a surge outflowing from the upper brightening. Surges are relatively cool outflows sometimes observed in conjunction with EBs and UVBs, driven by the magnetic reconnection process (e.g., Watanabe et al. 2011; Nóbrega-Siverio et al. 2021). Similar features have also been reproduced in simulations (Hansteen et al. 2019). This suggests fast-moving, cool gas at higher-than-average altitudes, which cannot be modeled under a plane-parallel atmosphere in hydrostatic equilibrium.

Microturbulence is also greatly enhanced in the brightening, particularly around $\log \tau = -3$, showing a mean(max) value of $\sim 5(14) \text{ km s}^{-1}$ while the FOV average is $\sim 0.4 \text{ km s}^{-1}$. Interestingly, this enhancement occurs in higher layers than the temperature enhancements, as exemplified by the profiles at locations (A) and (B) in Fig. 6. Although we find both increased Doppler shifts and microturbulence in the brightenings, there is no correlation between their magnitudes at any optical depth.

4.2.3. Challenges in Line Fitting

The strongest ViSP lines were generally very well fitted in the quiet areas of the FOV, where simple absorption profiles make further discussion unnecessary. The examples displayed in Fig. 6 also show generally good fits to the $\lambda 5896$ and $\lambda 8542$ line profiles in the brightenings. Locations showing strong Doppler shifted emission or absorption in $\lambda 8542$ were more challenging to fit even if we increased the number of nodes, causing some incompatibilities in the $\lambda 5896$ modeling, specifically forcing the sodium line to be brighter than observed (e.g., location B). In addition, several weaker photospheric lines, which were not included in the inversion process, show varying degrees of reproducibility. For example, the Ni I 5893 Å is relatively well reproduced in both intensity and circular polarization, whereas the Fe I line, blended in its blue wing, is clearly too deep in the observations compared to the model predictions. The polarization signals in the Si I and Fe I in the blue wing of $\lambda 8542$ are also systematically underestimated across the FOV. While these discrepancies do not impact the inversion results presented here, further investigation is required to identify the sources of these systematic errors so that these additional spectral diagnostics can also be utilized in the future.

4.3. Extrapolated Magnetic Configuration

Figure 7 shows the extrapolated magnetic field lines from the photospheric vector magnetograms, including a volume rendering of the squashing factor (yellow shade, (a)–(b)). We also show a vertical slice of the field curvature (c) and twist number (d). The visualization was created using VAPOR (Li et al. 2019b). The red field lines outline a low-lying dome structure connected to a spine, resembling a fan-spine or "anemone jet" configuration (e.g., Yokoyama & Shibata 1995; Shibata et al. 2007). This dome structure is also

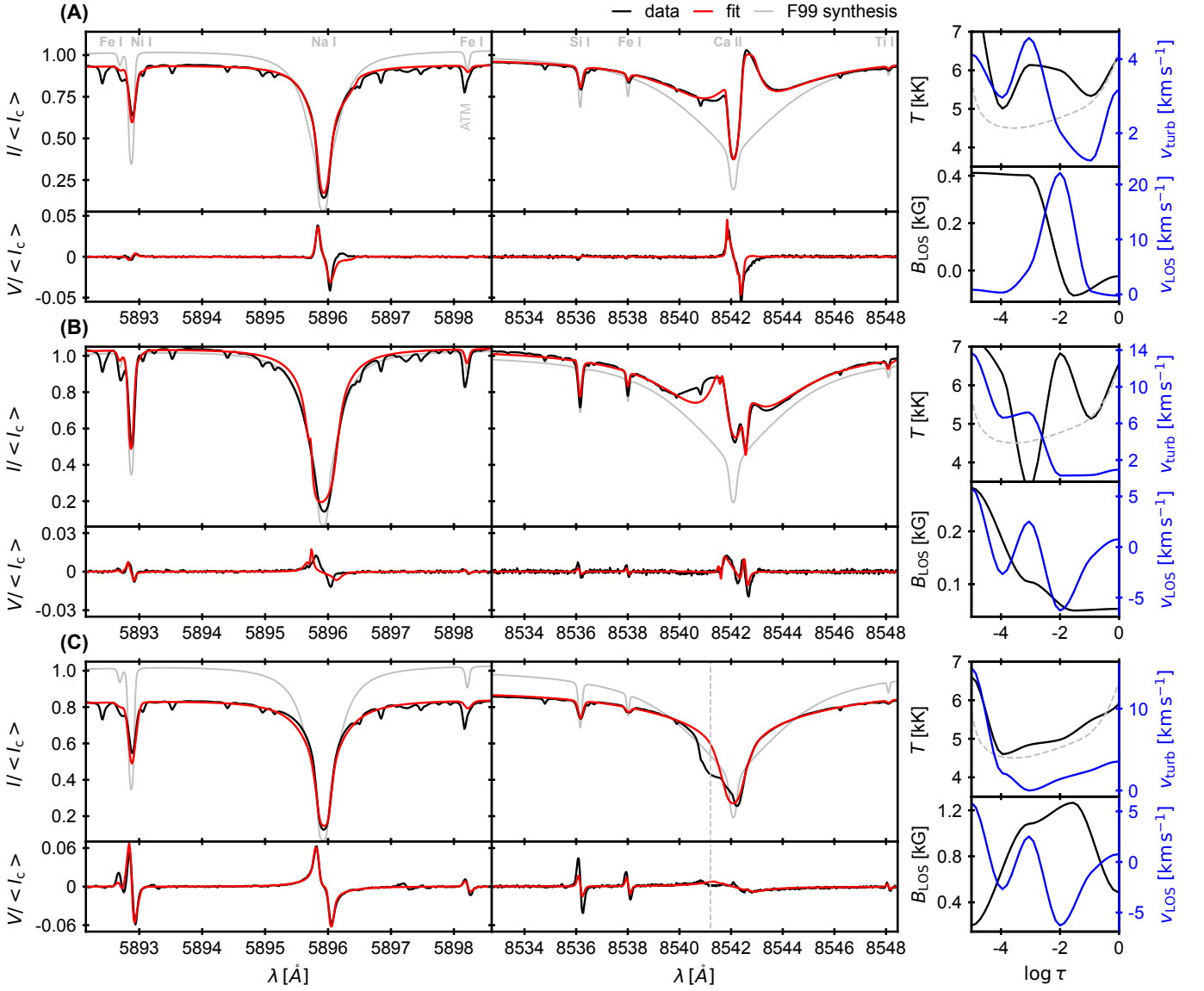


Figure 6. Spectra and best models at different locations. The three sets of panels show the observed ViSP spectra and best-fit models (left panels), as well as the corresponding model parameters as a function of logarithmic continuum optical depth (right panels)) at the three locations designated (A), (B), and (C) in Fig. 5. The gray dashed line in (C) indicates the position of the misfitted component at -31 km s^{-1} relative to the nominal line center. The gray solid lines in the left panels show the synthetic spectra computed from the F99 model, whose temperature profile is shown on the right panels (dashed line) for comparison with the targets’ profiles.

evident in the curvature map (c), showing a transition from a compact region with negative (concave) curvature to positive curvature above it. From the variation of the sign of the field curvature with height ($\hat{B} \cdot \nabla \hat{B}_z$), we determine the dome height to extend up to $\sim 700 \text{ km}$ above the photospheric layer, which is within the expected formation height range of $\lambda 8542$. The extrapolated field strength is on the order of 300 G or less at that height, consistent with the inferred magnetic field from the NLTE inversions around $\log \tau \sim -4.5$ within the uncertainties. This compact dome is also consistent with the small negative polarity field patch vanishing from the inversion maps quickly with height (cf. Fig. 5).

A magnetic null point was identified $\sim 500 \text{ km}$ above the extrapolation’s lower boundary, located between the two opposite polarities on one side of the dome and connecting to the spine. The projection of this null-point on the $z = 0$ plane coincides with the EB brightenings and lower part of the bright annular structure; however, it alone cannot fully explain the event’s complex morphology. Specifically, the bright fibril-like (and jet-like) structures oriented toward northeast (and east) in the Ca II K images (e.g., Fig. 3, 20:38 UT), are positioned a few arcseconds away from the null point and are not aligned along the main spine but rather at an angle to it. The dark outflows observed in $\lambda 8542$ (cf.

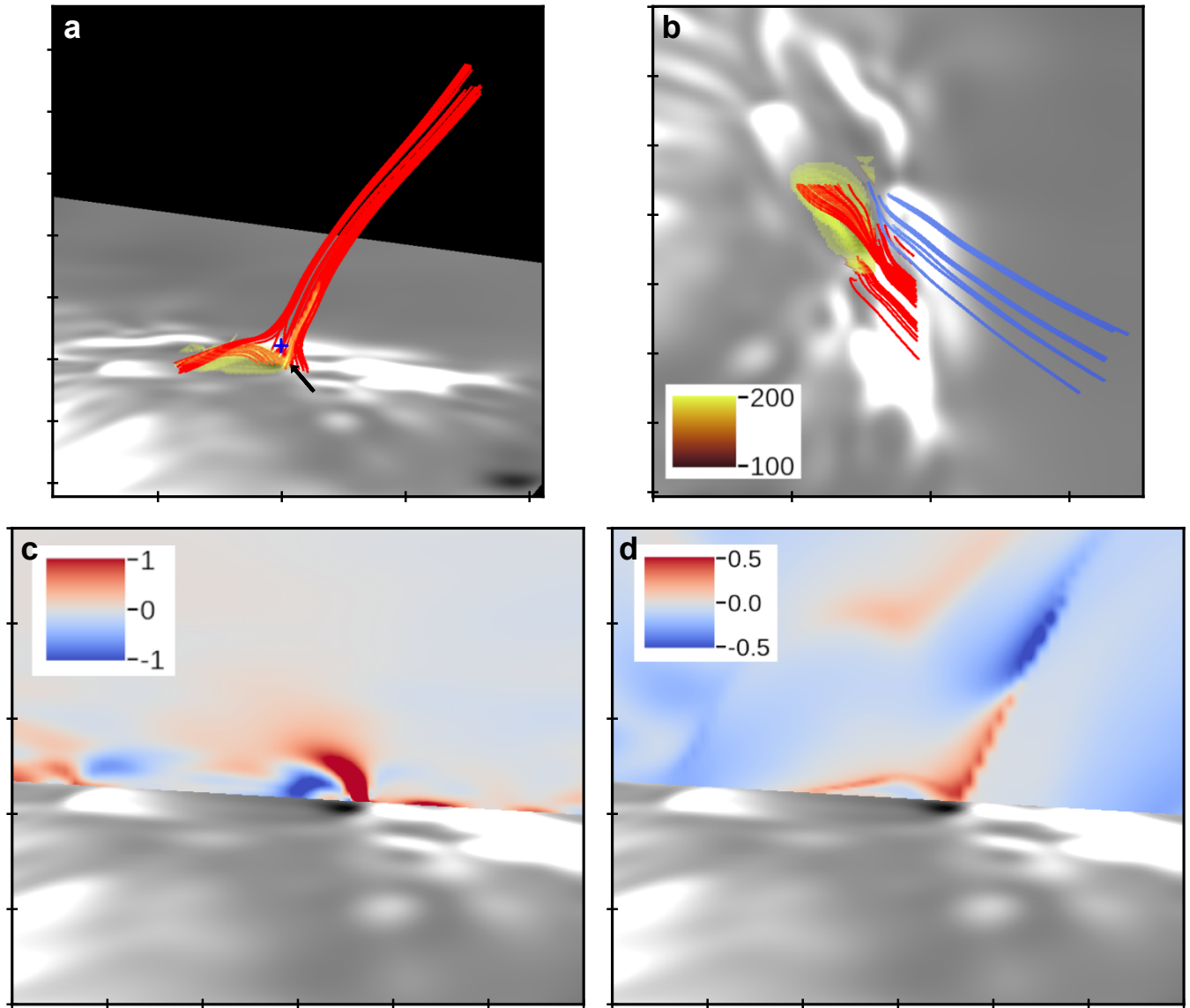


Figure 7. Magnetic field extrapolation with the NLFFF method. (a): Side view of the ROI showing the traced field lines (red), and a volume rendering of the squashing factor (yellow); the blue cross shows the location of the magnetic null point, located ~ 500 km above the magnetogram displayed at the lower boundary (capped at ± 700 G.). (b): Top view of the ROI, including blue field lines traced from the footpoints of the surge observed in the core of $\lambda 8542$ (cf. Fig. 5). (c): Vertical slice of the field curvature. (d): Vertical slice of the twist number. All colormaps are capped for display purposes.

Fig. 5) are also shifted by $\sim 1-2''$ to the north relative to the main spine. The blue-colored field lines in this region indicate that the inferred topology roughly follows the orientation of the surge-like features. It is plausible that reconnection occurs at multiple locations across the structure that are not necessarily null points.

The squashing factor, Q , also shows a low-lying dome-like structure. High Q values (a few $\sim 10^2$) are concentrated along the boundaries of the dome, indicating sharp gradients in magnetic field connectivity. These regions are quasi-separatrix layers (QSLs), where magnetic reconnection can occur (e.g., Priest & Démoulin 1995; Titov et al. 2002).

The QSL encloses the fan field lines, while the spine extends through the dome's top. The current density is also enhanced around the dome in a semi-circular region below 1 Mm in height tracing the PIL (not displayed). The highest Q values ($\sim 10^3 - 10^4$) appear in an extended, narrow sheet (black arrow) that stretches 1.4 Mm upward from the boundary along the spine between the two opposite polarities. This region also coincides with the location of the $H\beta$ brightenings.

The twist number map shows localized enhancements between the two polarities, possibly due to shearing or rotational motions of the dome/spine footpoints. This may contribute to magnetic stress buildup, leading to high Q values.

While the twist numbers are generally small ($|\mathcal{T}_w| \lesssim 0.8$), a clear transition from negative to positive twist occurs with height at the dome and along the spine.

We note that the ViSP only captured a narrow time interval of a series of recurrent brightenings at the same location, as shown in Fig. 2 and Fig. 3. These successive brightenings may have driven the magnetic structure into a lower-energy state at this instance. Note that the extrapolation requires a trade-off between the observed photospheric magnetic field and the force-free assumption, resulting in an intrinsically smoother modeled boundary condition (Fig. 7). Additionally, the extrapolated field may not fully capture certain aspects of the field configuration, given the low cadence of the ViSP raster relative to the rapid timescale of the event.

5. DISCUSSION AND CONCLUSIONS

In this paper, we present high-resolution observations of a series of brightenings in an active region near the solar disk center. We interpret them as the result of a low-altitude, small-scale magnetic reconnection event occurring as part of a long-lived flux cancellation process. We observe a steady decrease in magnetic flux observed in HMI magnetograms over an hour and recurrent 1700 Å continuum enhancements at the same location. Although the ViSP raster captured only a brief, few-minute snapshot of this process, it enabled the detection of strong Doppler shifts and increased microturbulence in spectral lines probing the upper photosphere and low chromosphere. The velocity magnitudes are comparable to the local Alfvén speed, consistent with reconnection-driven flows (e.g., Pontin & Priest 2022).

The broadband VBI images reveal EB-like flickering emissions and compact blobs in $H\beta$, whereas Ca II K shows a more extended bright annular structure, hot jet-like outflows, and cooler surges. Previous observations have shown bright substructures in magnetic reconnection events, suggesting plasmoid-mediated intermittent reconnection (e.g., Innes et al. 2015; Rouppe van der Voort et al. 2017; Díaz Baso et al. 2021; Leenaarts et al. 2025), or energy deposition in small-scale magnetic loops (Smitha et al. 2018). In the $H\beta$ image sequence, we observe structures that align with the plasmoid interpretation. However, these structures may not necessarily be magnetic islands; they could instead be hot, over-dense regions driven by shocks and/or turbulence, emitting strongly in $H\beta$. Discriminating between these scenarios requires higher-cadence (<30 s) and higher-sensitivity magnetometry, which is a technical challenge for slit-based spectropolarimeters like the ViSP. The bright $H\beta$ blobs are likely obscured by the overlying chromospheric canopy, which is more opaque in Ca II K, hence their absence in that filter.

These observations suggest a more complex magnetic topology than that of classical EBs (e.g., Rutten et al. 2013) resembling cases in Bhatnagar et al. (2024). In that study,

some QS EBs were found to have UV emission counterparts originating from different parts of fan-spine structures, as revealed by magnetic field extrapolations. Similarly, some AR EBs also have UVB counterparts in IRIS data, which can be spatially offset or display different characteristics (e.g., Visers et al. 2015; Tian et al. 2016; Chen et al. 2019; Ortiz et al. 2020). However, at a spatial resolution of ~ 0.33 – $0.4''$, IRIS brightenings typically appear compact (or dot-like), elongated, or surge-like (e.g., Tiwari et al. 2019), and bright annular structures have not yet been reported. Given the $\sim 0.11''$ width of the observed annulus, resolving such features in IRIS images would be challenging. Co-observations with IRIS are needed to explore potential UV spectral signatures. Regardless of the event classification, these observations provide further evidence of the various ways in which magnetic reconnection can occur in the solar atmosphere (reviewed in Janvier 2017; Pontin & Priest 2022).

This interpretation is further supported by a multi-resolution NLFFF extrapolation based on a combination of HMI and ViSP magnetograms. The magnetic topology resembles a fan-spine configuration with a null point ~ 500 km above the photosphere. Coincidentally, our height estimate matches that provided by Chitta et al. (2017) where a Si IV 1400 Å UVB observed by IRIS coincided with a null-point location in a fan-spine structure. However, in our case, brightenings extend beyond the null, suggesting a different origin. We also find enhanced squashing factors within a low-lying, dome-shaped structure surrounding the negative polarity patch, extending up to ~ 0.7 Mm in height, as well as within an extended thin sheet between the two opposite polarities, reaching up to ~ 1.4 Mm. These regions define QSLs, where three-dimensional reconnection can occur without null points through continuous magnetic field line slippage (e.g., Priest & Démoulin 1995; Démoulin et al. 1996). The bright ring-like structure and its central brightening may correspond to a two-dimensional cross-section of a heated magnetic dome, with radiative cooling rates being higher in relatively deeper layers of the upper photosphere and low chromosphere around the dome than at its apex.

The continuous inflow of magnetic bright elements at relatively high speeds (~ 4 – 6 km s $^{-1}$) to the region, as observed in the G-band image sequences when the ring appears (compared to their absence earlier in the time series), suggests that they may have contributed to significant magnetic field gradients, including field twist. This likely stressed the magnetic structure and led to enhanced squashing factors. Furthermore, the motions of the G-band bright points appear to mimic variations in the annular diameter and orientation, with a misalignment likely due to projection effects. Therefore, reconnection at QSLs plausibly explains the annular emissions (see also Pariat et al. 2004; Tian et al. 2018), with physical variations of the QSL due to magnetic reconnection

and force rebalancing and/or motions by the photospheric bright points potentially explaining the temporal variations in the Ca II K ring size and orientation. This process unfolded in a region already undergoing flux cancellation, as shown by the persistent EB-like H β brightenings between the opposite magnetic polarities before the ring became visible.

The spatial coherence and smoothness of the annular emissions could also indicate heating by nonthermal particles. In this scenario, magnetic reconnection directs nonthermal electrons along dome field lines, producing a ring-like emission pattern as they collide with the dense lower atmosphere. This could also explain the strong downflows (interpreted as condensations), line profile asymmetries, and enhanced microturbulence (up to $\sim 14 \text{ km s}^{-1}$) in the region. Bright ring-like features have been observed in circular flare ribbons within fan-spine configurations (e.g., [Masson et al. 2009](#); [Sun et al. 2013](#)), though on much larger physical scales. Similar enhancements in microturbulence (or nonthermal broadening) occur in chromospheric flare ribbons/kernels (e.g., [Yadav et al. 2021](#); [Sainz Dalda & De Pontieu 2023](#); [Kerr et al. 2024](#)). This event may represent a small-scale, low-altitude analogue involving nonthermal particles, as even the weakest flares (microflares and nanoflares) can exhibit significant nonthermal effects in the low chromosphere (e.g., [Testa et al. 2014, 2023](#); [Cho et al. 2023](#)). Nonthermal models have also been considered to explain EB spectral signatures (e.g., [Fang et al. 2006](#); [Hong et al. 2017](#)). In our case, the absence of an obvious coronal source suggests that the nonthermal electrons must be generated within the low chromosphere and would not travel far. The distance electrons travel from the reconnection site to the energy deposition location is largely dependent on the density and the electron energy (e.g., [Bakke et al. 2023](#)). In this case, the projected distance is a few hundred kilometers. Simulations have also shown that different chromospheric lines respond differently to the electron flux in nonthermal models (e.g., [Hong et al. 2017](#); [Bakke et al. 2022, 2023](#)), with the Ca II H and K lines often exhibiting stronger responses than the H I Balmer lines. This may explain why we observe such distinct structures in Ca II K and H β VBI filter images, as thermal effects would be more likely to affect different lines in a similar manner. However, existing models have yet to fully reproduce the observed spectra (e.g., [Testa et al. 2023](#)).

Regarding the inferred temperatures in the EB, both the $\lambda 5896$ and $\lambda 8542$ lines can be well reproduced without requiring a highly localized temperature hump ($\lesssim 20 \text{ km}$) in the upper photosphere ([Seo et al. 2019](#)). These lines can be well fitted with relatively broad temperature peaks ($\Delta T \sim 1 \text{ kK}$) over a range of optical depths corresponding to a couple

hundred kilometers assuming hydrostatic equilibrium. However, the high downflow speeds inferred at the EB locations ($\sim 20 \text{ km s}^{-1}$) may slightly increase the effective gravity and decrease the pressure scale height. Notably, the event remains invisible in sodium line intensities. However, according to our models, this does not necessarily imply temperatures high enough to fully ionize the neutral species in those layers ($\gtrsim 10 \text{ kK}$, [Rutten et al. 2015](#); [Rutten 2016](#)). In contrast, observations in He I 10830 \AA show that significantly higher temperatures ($\gtrsim 20 \text{ kK}$) than the ones inferred here occur in some EBs deep in the atmosphere ([Libbrecht et al. 2017](#); [Leenaarts et al. 2025](#)), beyond the sensitivity range of the Na I and Ca II lines.

These results underscore the intricate nature of small-scale reconnection events in ARs and their impact on the lower solar atmosphere. Further high-cadence and multi-wavelength observations, combined with advanced modeling, will be essential to disentangle the thermal and nonthermal contributions to these processes and to improve reconstructions of the magnetic field topology, particularly through multi-layer extrapolations ([Jarolim et al. 2024a](#)).

The research reported herein is based in part on data collected with the Daniel K. Inouye Solar Telescope (DKIST), a facility of the National Solar Observatory (NSO). DKIST is located on land of spiritual and cultural significance to Native Hawaiian people. The use of this important site to further scientific knowledge is done so with appreciation and respect. The NSO is operated by the Association of Universities for Research in Astronomy, Inc., under cooperative agreement with the National Science Foundation. This research was supported by the National Science Foundation REU program, Award #1950911. This work utilized the Blanca condo computing resource and the Alpine high performance computing resource at the University of Colorado Boulder. Blanca is jointly funded by computing users and the University of Colorado Boulder. Alpine is jointly funded by the University of Colorado Boulder, the University of Colorado Anschutz, and Colorado State University. This project has received funding from the Swedish Research Council (2021-05613) and the Swedish National Space Agency (2021-00116).

Facilities: SDO(AIA & HMI), DKIST(ViSP & VBI)

Software: Astropy ([Astropy Collaboration et al. 2013, 2018](#)), Sunpy ([The SunPy Community et al. 2020](#)), pyMilne ([de la Cruz Rodríguez 2019](#)), STiC ([de la Cruz Rodríguez et al. 2019](#)), NF2 ([Jarolim et al. 2023](#)), FastQSL ([Zhang et al. 2022](#)), VAPOR ([Li et al. 2019b](#))

APPENDIX

A. SUPPLEMENTAL MOVIE

REFERENCES

- Anan, T., Casini, R., Uitenbroek, H., et al. 2024, *Nature Communications*, 15, 8811, doi: [10.1038/s41467-024-53102-x](https://doi.org/10.1038/s41467-024-53102-x)
- Astropy Collaboration, Robitaille, T. P., Tollerud, E. J., et al. 2013, *A&A*, 558, A33, doi: [10.1051/0004-6361/201322068](https://doi.org/10.1051/0004-6361/201322068)
- Astropy Collaboration, Price-Whelan, A. M., Sipőcz, B. M., et al. 2018, *AJ*, 156, 123, doi: [10.3847/1538-3881/aabc4f](https://doi.org/10.3847/1538-3881/aabc4f)
- Bakke, H., Carlsson, M., Rouppe van der Voort, L., et al. 2022, *A&A*, 659, A186, doi: [10.1051/0004-6361/202142842](https://doi.org/10.1051/0004-6361/202142842)
- Bakke, H., Frogner, L., Rouppe van der Voort, L., Gudiksen, B. V., & Carlsson, M. 2023, *A&A*, 675, A103, doi: [10.1051/0004-6361/202346765](https://doi.org/10.1051/0004-6361/202346765)
- Berger, M. A., & Prior, C. 2006, *Journal of Physics A Mathematical General*, 39, 8321, doi: [10.1088/0305-4470/39/26/005](https://doi.org/10.1088/0305-4470/39/26/005)
- Bhatnagar, A., Prasad, A., Rouppe van der Voort, L., Nóbrega-Siverio, D., & Joshi, J. 2024, arXiv e-prints, arXiv:2412.03211, doi: [10.48550/arXiv.2412.03211](https://doi.org/10.48550/arXiv.2412.03211)
- Bobra, M. G., Sun, X., Hoeksema, J. T., et al. 2014, *SoPh*, 289, 3549, doi: [10.1007/s11207-014-0529-3](https://doi.org/10.1007/s11207-014-0529-3)
- Chen, Y., Tian, H., Peter, H., et al. 2019, *ApJL*, 875, L30, doi: [10.3847/2041-8213/ab18a4](https://doi.org/10.3847/2041-8213/ab18a4)
- Chitta, L. P., & Lazarian, A. 2020, *ApJL*, 890, L2, doi: [10.3847/2041-8213/ab6f0a](https://doi.org/10.3847/2041-8213/ab6f0a)
- Chitta, L. P., Peter, H., Priest, E. R., & Solanki, S. K. 2020, *A&A*, 644, A130, doi: [10.1051/0004-6361/202039099](https://doi.org/10.1051/0004-6361/202039099)
- Chitta, L. P., Peter, H., Young, P. R., & Huang, Y. M. 2017, *A&A*, 605, A49, doi: [10.1051/0004-6361/201730830](https://doi.org/10.1051/0004-6361/201730830)
- Cho, K., Testa, P., De Pontieu, B., & Polito, V. 2023, *ApJ*, 945, 143, doi: [10.3847/1538-4357/acb7da](https://doi.org/10.3847/1538-4357/acb7da)
- da Silva Santos, J. M., de la Cruz Rodríguez, J., White, S. M., et al. 2020, *A&A*, 643, A41, doi: [10.1051/0004-6361/202038755](https://doi.org/10.1051/0004-6361/202038755)
- da Silva Santos, J. M., Molnar, M., Milić, I., et al. 2024, *ApJ*, 976, 21
- Danilovic, S. 2017, *A&A*, 601, A122, doi: [10.1051/0004-6361/201730403](https://doi.org/10.1051/0004-6361/201730403)
- Danilovic, S., Solanki, S. K., Barthol, P., et al. 2017, *ApJS*, 229, 5, doi: [10.3847/1538-4365/229/1/5](https://doi.org/10.3847/1538-4365/229/1/5)
- de la Cruz Rodríguez, J. 2019, *A&A*, 631, A153, doi: [10.1051/0004-6361/201936635](https://doi.org/10.1051/0004-6361/201936635)
- de la Cruz Rodríguez, J., Leenaarts, J., & Asensio Ramos, A. 2016, *ApJL*, 830, L30, doi: [10.3847/2041-8205/830/2/L30](https://doi.org/10.3847/2041-8205/830/2/L30)
- de la Cruz Rodríguez, J., Leenaarts, J., Danilovic, S., & Uitenbroek, H. 2019, *A&A*, 623, A74, doi: [10.1051/0004-6361/201834464](https://doi.org/10.1051/0004-6361/201834464)
- de Wijn, A. G., Casini, R., Carlile, A., et al. 2022, *SoPh*, 297, 22, doi: [10.1007/s11207-022-01954-1](https://doi.org/10.1007/s11207-022-01954-1)
- Démoulin, P., Priest, E. R., & Lonie, D. P. 1996, *J. Geophys. Res.*, 101, 7631, doi: [10.1029/95JA03558](https://doi.org/10.1029/95JA03558)
- Díaz Baso, C. J., de la Cruz Rodríguez, J., & Leenaarts, J. 2021, *A&A*, 647, A188, doi: [10.1051/0004-6361/202040111](https://doi.org/10.1051/0004-6361/202040111)
- Dunn, R. B., & Zirker, J. B. 1973, *SoPh*, 33, 281, doi: [10.1007/BF00152419](https://doi.org/10.1007/BF00152419)
- Ellerman, F. 1917, *ApJ*, 46, 298, doi: [10.1086/142366](https://doi.org/10.1086/142366)
- Fang, C., Tang, Y. H., Xu, Z., Ding, M. D., & Chen, P. F. 2006, *ApJ*, 643, 1325, doi: [10.1086/501342](https://doi.org/10.1086/501342)
- Fontenla, J., White, O. R., Fox, P. A., Avrett, E. H., & Kurucz, R. L. 1999, *ApJ*, 518, 480, doi: [10.1086/307258](https://doi.org/10.1086/307258)
- Freeland, S. L., & Handy, B. N. 1998, *SoPh*, 182, 497, doi: [10.1023/A:1005038224881](https://doi.org/10.1023/A:1005038224881)
- Georgoulis, M. K., Rust, D. M., Bernasconi, P. N., & Schmieder, B. 2002, *ApJ*, 575, 506, doi: [10.1086/341195](https://doi.org/10.1086/341195)
- Hagenaar, H. J., & Shine, R. A. 2005, *ApJ*, 635, 659, doi: [10.1086/497367](https://doi.org/10.1086/497367)
- Hansteen, V., Ortiz, A., Archontis, V., et al. 2019, *A&A*, 626, A33, doi: [10.1051/0004-6361/201935376](https://doi.org/10.1051/0004-6361/201935376)
- Hansteen, V. H., Archontis, V., Pereira, T. M. D., et al. 2017, *ApJ*, 839, 22, doi: [10.3847/1538-4357/aa6844](https://doi.org/10.3847/1538-4357/aa6844)
- Hong, J., Carlsson, M., & Ding, M. D. 2017, *ApJ*, 845, 144, doi: [10.3847/1538-4357/aa80e3](https://doi.org/10.3847/1538-4357/aa80e3)
- Innes, D. E., Guo, L. J., Huang, Y. M., & Bhattacharjee, A. 2015, *ApJ*, 813, 86, doi: [10.1088/0004-637X/813/2/86](https://doi.org/10.1088/0004-637X/813/2/86)
- Janvier, M. 2017, *Journal of Plasma Physics*, 83, 535830101, doi: [10.1017/S0022377817000034](https://doi.org/10.1017/S0022377817000034)
- Jarolim, R., Thalmann, J. K., Veronig, A. M., & Podladchikova, T. 2023, *Nature Astronomy*, doi: [10.1038/s41550-023-02030-9](https://doi.org/10.1038/s41550-023-02030-9)
- Jarolim, R., Tremblay, B., Rempel, M., et al. 2024a, *ApJL*, 963, L21, doi: [10.3847/2041-8213/ad2450](https://doi.org/10.3847/2041-8213/ad2450)
- Jarolim, R., Veronig, A. M., Purkhart, S., Zhang, P., & Rempel, M. 2024b, *ApJL*, 976, L12, doi: [10.3847/2041-8213/ad8914](https://doi.org/10.3847/2041-8213/ad8914)
- Joshi, J., Rouppe van der Voort, L. H. M., & de la Cruz Rodríguez, J. 2020, *A&A*, 641, L5, doi: [10.1051/0004-6361/202038769](https://doi.org/10.1051/0004-6361/202038769)
- Kerr, G. S., Kowalski, A. F., Allred, J. C., Daw, A. N., & Kane, M. R. 2024, *MNRAS*, 527, 2523, doi: [10.1093/mnras/stad3135](https://doi.org/10.1093/mnras/stad3135)

- Korsós, M. B., Jarolim, R., Erdélyi, R., et al. 2024, *ApJ*, 962, 171, doi: [10.3847/1538-4357/ad18bd](https://doi.org/10.3847/1538-4357/ad18bd)
- Leenaarts, J., van Noort, M., de la Cruz Rodríguez, J., et al. 2025, arXiv e-prints, arXiv:2501.10246, doi: [10.48550/arXiv.2501.10246](https://doi.org/10.48550/arXiv.2501.10246)
- Leka, K. D., Barnes, G., & Crouch, A. 2014, AMBIG: Automated Ambiguity-Resolution Code, Astrophysics Source Code Library, record ascl:1404.007
- Lemen, J. R., Title, A. M., Akin, D. J., et al. 2012, *SoPh*, 275, 17, doi: [10.1007/s11207-011-9776-8](https://doi.org/10.1007/s11207-011-9776-8)
- Li, Q., Deng, N., Jing, J., Liu, C., & Wang, H. 2019a, *ApJ*, 876, 129, doi: [10.3847/1538-4357/ab18aa](https://doi.org/10.3847/1538-4357/ab18aa)
- Li, S., Jaroszynski, S., Pearse, S., Orf, L., & Clyne, J. 2019b, *Atmosphere*, 10, 488, doi: [10.3390/atmos10090488](https://doi.org/10.3390/atmos10090488)
- Libbrecht, T., Joshi, J., de la Cruz Rodríguez, J., Leenaarts, J., & Ramos, A. A. 2017, *A&A*, 598, A33, doi: [10.1051/0004-6361/201629266](https://doi.org/10.1051/0004-6361/201629266)
- Masson, S., Pariat, E., Aulanier, G., & Schrijver, C. J. 2009, *ApJ*, 700, 559, doi: [10.1088/0004-637X/700/1/559](https://doi.org/10.1088/0004-637X/700/1/559)
- McKevitt, J., Jarolim, R., Matthews, S., et al. 2024, *ApJL*, 961, L29, doi: [10.3847/2041-8213/ad1bee](https://doi.org/10.3847/2041-8213/ad1bee)
- Morosin, R., de la Cruz Rodríguez, J., Vissers, G. J. M., & Yadav, R. 2020, *A&A*, 642, A210, doi: [10.1051/0004-6361/202038754](https://doi.org/10.1051/0004-6361/202038754)
- Neckel, H., & Labs, D. 1984, *SoPh*, 90, 205, doi: [10.1007/BF00173953](https://doi.org/10.1007/BF00173953)
- Nóbrega-Siverio, D., Guglielmino, S. L., & Sainz Dalda, A. 2021, *A&A*, 655, A28, doi: [10.1051/0004-6361/202141472](https://doi.org/10.1051/0004-6361/202141472)
- Ortiz, A., Hansteen, V. H., Nóbrega-Siverio, D., & Rouppe van der Voort, L. 2020, *A&A*, 633, A58, doi: [10.1051/0004-6361/201936574](https://doi.org/10.1051/0004-6361/201936574)
- Pariat, E., Aulanier, G., Schmieder, B., et al. 2004, *ApJ*, 614, 1099, doi: [10.1086/423891](https://doi.org/10.1086/423891)
- Pariat, E., Masson, S., & Aulanier, G. 2009, *ApJ*, 701, 1911, doi: [10.1088/0004-637X/701/2/1911](https://doi.org/10.1088/0004-637X/701/2/1911)
- Pesnell, W. D., Thompson, B. J., & Chamberlin, P. C. 2012, *SoPh*, 275, 3, doi: [10.1007/s11207-011-9841-3](https://doi.org/10.1007/s11207-011-9841-3)
- Peter, H., Huang, Y. M., Chitta, L. P., & Young, P. R. 2019, *A&A*, 628, A8, doi: [10.1051/0004-6361/201935820](https://doi.org/10.1051/0004-6361/201935820)
- Peter, H., Tian, H., Curdt, W., et al. 2014, *Science*, 346, 1255726, doi: [10.1126/science.1255726](https://doi.org/10.1126/science.1255726)
- Pontin, D. I., & Priest, E. R. 2022, *Living Reviews in Solar Physics*, 19, 1, doi: [10.1007/s41116-022-00032-9](https://doi.org/10.1007/s41116-022-00032-9)
- Priest, E. R., & Démoulin, P. 1995, *J. Geophys. Res.*, 100, 23443, doi: [10.1029/95JA02740](https://doi.org/10.1029/95JA02740)
- Purkhart, S., Veronig, A. M., Dickson, E. C. M., et al. 2023, *A&A*, 679, A99, doi: [10.1051/0004-6361/202346354](https://doi.org/10.1051/0004-6361/202346354)
- Raissi, M., Perdikaris, P., & Karniadakis, G. E. 2019, *Journal of Computational Physics*, 378, 686, doi: [10.1016/j.jcp.2018.10.045](https://doi.org/10.1016/j.jcp.2018.10.045)
- Reardon, K. P. 2006, *SoPh*, 239, 503, doi: [10.1007/s11207-006-0283-2](https://doi.org/10.1007/s11207-006-0283-2)
- Reid, A., Mathioudakis, M., Doyle, J. G., et al. 2016, *ApJ*, 823, 110, doi: [10.3847/0004-637X/823/2/110](https://doi.org/10.3847/0004-637X/823/2/110)
- Rimmele, T. R., Warner, M., Keil, S. L., et al. 2020, *SoPh*, 295, 172, doi: [10.1007/s11207-020-01736-7](https://doi.org/10.1007/s11207-020-01736-7)
- Rouppe van der Voort, L., De Pontieu, B., Scharmer, G. B., et al. 2017, *ApJL*, 851, L6, doi: [10.3847/2041-8213/aa99dd](https://doi.org/10.3847/2041-8213/aa99dd)
- Rouppe van der Voort, L. H. M., van Noort, M., & de la Cruz Rodríguez, J. 2023, *A&A*, 673, A11, doi: [10.1051/0004-6361/202345933](https://doi.org/10.1051/0004-6361/202345933)
- Rutten, R. J. 2016, *A&A*, 590, A124, doi: [10.1051/0004-6361/201526489](https://doi.org/10.1051/0004-6361/201526489)
- Rutten, R. J., Rouppe van der Voort, L. H. M., & Vissers, G. J. M. 2015, *ApJ*, 808, 133, doi: [10.1088/0004-637X/808/2/133](https://doi.org/10.1088/0004-637X/808/2/133)
- Rutten, R. J., Vissers, G. J. M., Rouppe van der Voort, L. H. M., Sütterlin, P., & Vitas, N. 2013, in *Journal of Physics Conference Series*, Vol. 440, *Journal of Physics Conference Series (IOP)*, 012007, doi: [10.1088/1742-6596/440/1/012007](https://doi.org/10.1088/1742-6596/440/1/012007)
- Sainz Dalda, A., & De Pontieu, B. 2023, *Frontiers in Astronomy and Space Sciences*, 10, 1133429, doi: [10.3389/fspas.2023.1133429](https://doi.org/10.3389/fspas.2023.1133429)
- Sanchez Almeida, J., & Lites, B. W. 1992, *ApJ*, 398, 359, doi: [10.1086/171861](https://doi.org/10.1086/171861)
- Schad, T. A., Tritschler, A., & Cauzzi, G. 2025, arXiv e-prints, arXiv:2502.02742. <https://arxiv.org/abs/2502.02742>
- Scherrer, P. H., Schou, J., Bush, R. I., et al. 2012, *Sol. Phys.*, 275, 207
- Seo, M., Quintero Noda, C., Lee, J., & Chae, J. 2019, *ApJ*, 871, 125, doi: [10.3847/1538-4357/aaf55f](https://doi.org/10.3847/1538-4357/aaf55f)
- Shibata, K., Nakamura, T., Matsumoto, T., et al. 2007, *Science*, 318, 1591, doi: [10.1126/science.1146708](https://doi.org/10.1126/science.1146708)
- Skan, M., Danilovic, S., Leenaarts, J., Calvo, F., & Rempel, M. 2023, *A&A*, 672, A47, doi: [10.1051/0004-6361/202245390](https://doi.org/10.1051/0004-6361/202245390)
- Smitha, H. N., Chitta, L. P., Wiegelmann, T., & Solanki, S. K. 2018, *A&A*, 617, A128, doi: [10.1051/0004-6361/201833276](https://doi.org/10.1051/0004-6361/201833276)
- Sun, X., Hoeksema, J. T., Liu, Y., et al. 2013, *ApJ*, 778, 139, doi: [10.1088/0004-637X/778/2/139](https://doi.org/10.1088/0004-637X/778/2/139)
- Testa, P., Bakke, H., Rouppe van der Voort, L., & De Pontieu, B. 2023, *ApJ*, 956, 85, doi: [10.3847/1538-4357/acf4f1](https://doi.org/10.3847/1538-4357/acf4f1)
- Testa, P., De Pontieu, B., Allred, J., et al. 2014, *Science*, 346, 1255724, doi: [10.1126/science.1255724](https://doi.org/10.1126/science.1255724)
- The SunPy Community, Barnes, W. T., Bobra, M. G., et al. 2020, *The Astrophysical Journal*, 890, 68, doi: [10.3847/1538-4357/ab4f7a](https://doi.org/10.3847/1538-4357/ab4f7a)
- Tian, H., Xu, Z., He, J., & Madsen, C. 2016, *ApJ*, 824, 96, doi: [10.3847/0004-637X/824/2/96](https://doi.org/10.3847/0004-637X/824/2/96)
- Tian, H., Zhu, X., Peter, H., et al. 2018, *ApJ*, 854, 174, doi: [10.3847/1538-4357/aaaac6](https://doi.org/10.3847/1538-4357/aaaac6)
- Titov, V. S. 2007, *ApJ*, 660, 863, doi: [10.1086/512671](https://doi.org/10.1086/512671)

- Titov, V. S., Hornig, G., & Démoulin, P. 2002, *Journal of Geophysical Research (Space Physics)*, 107, 1164, doi: [10.1029/2001JA000278](https://doi.org/10.1029/2001JA000278)
- Titov, V. S., Priest, E. R., & Demoulin, P. 1993, *A&A*, 276, 564
- Tiwari, S. K., Panesar, N. K., Moore, R. L., et al. 2019, *ApJ*, 887, 56, doi: [10.3847/1538-4357/ab54c1](https://doi.org/10.3847/1538-4357/ab54c1)
- Uitenbroek, H. 2001, *ApJ*, 557, 389, doi: [10.1086/321659](https://doi.org/10.1086/321659)
- Vissers, G. J. M., Rouppe van der Voort, L. H. M., & Rutten, R. J. 2013, *ApJ*, 774, 32, doi: [10.1088/0004-637X/774/1/32](https://doi.org/10.1088/0004-637X/774/1/32)
- . 2019, *A&A*, 626, A4, doi: [10.1051/0004-6361/201834811](https://doi.org/10.1051/0004-6361/201834811)
- Vissers, G. J. M., Rouppe van der Voort, L. H. M., Rutten, R. J., Carlsson, M., & De Pontieu, B. 2015, *ApJ*, 812, 11, doi: [10.1088/0004-637X/812/1/11](https://doi.org/10.1088/0004-637X/812/1/11)
- Wang, H., & Liu, C. 2012, *ApJ*, 760, 101, doi: [10.1088/0004-637X/760/2/101](https://doi.org/10.1088/0004-637X/760/2/101)
- Watanabe, H., Vissers, G., Kitai, R., Rouppe van der Voort, L., & Rutten, R. J. 2011, *ApJ*, 736, 71, doi: [10.1088/0004-637X/736/1/71](https://doi.org/10.1088/0004-637X/736/1/71)
- Withbroe, G. L., & Noyes, R. W. 1977, *ARA&A*, 15, 363, doi: [10.1146/annurev.aa.15.090177.002051](https://doi.org/10.1146/annurev.aa.15.090177.002051)
- Wöger, F., Rimmele, T., Ferayorni, A., et al. 2021, *SoPh*, 296, 145, doi: [10.1007/s11207-021-01881-7](https://doi.org/10.1007/s11207-021-01881-7)
- Wöger, F., von der Lühe, O., & Reardon, K. 2008, *A&A*, 488, 375, doi: [10.1051/0004-6361:200809894](https://doi.org/10.1051/0004-6361:200809894)
- Wu, P. 2019, *ApJ*, 885, 158, doi: [10.3847/1538-4357/ab4a06](https://doi.org/10.3847/1538-4357/ab4a06)
- Yadav, R., Díaz Baso, C. J., de la Cruz Rodríguez, J., Calvo, F., & Morosin, R. 2021, *A&A*, 649, A106, doi: [10.1051/0004-6361/202039857](https://doi.org/10.1051/0004-6361/202039857)
- Yokoyama, T., & Shibata, K. 1995, *Nature*, 375, 42, doi: [10.1038/375042a0](https://doi.org/10.1038/375042a0)
- Young, P. R., Tian, H., Peter, H., et al. 2018, *SSRv*, 214, 120, doi: [10.1007/s11214-018-0551-0](https://doi.org/10.1007/s11214-018-0551-0)
- Zhang, P., Chen, J., Liu, R., & Wang, C. 2022, *ApJ*, 937, 26, doi: [10.3847/1538-4357/ac8d61](https://doi.org/10.3847/1538-4357/ac8d61)
- Zhao, J., Schmieder, B., Li, H., et al. 2017, *ApJ*, 836, 52, doi: [10.3847/1538-4357/836/1/52](https://doi.org/10.3847/1538-4357/836/1/52)